EES Batteries

Accepted Manuscript

This article can be cited before page numbers have been issued, to do this please use: S. Alvi, A. Fazi, D. Weber, D. Hedman, K. Choudhary, O. Bäcke, F. Akhtar, J. Chotard, M. Thuvander and P. Johansson, *EES Batteries*, 2026, DOI: 10.1039/D6EB00032K.

View Article Online
DOI: 10.1039/D6EB00032K

Broader Context

Market demand for high-energy density lithium-ion batteries continues to grow, in particular for application in circuit boards, electric aviation and electric vehicles. To meet these demands, alloy-engineered anodes have recently become of interest, with large promises of improved energy density. However, to truly become an alternative to the today dominant carbonaceous anodes, the effects of entropy and nano-level heterogeneity on the cycling performance needs to be investigated. We here address this knowledge gap by using tellurium-based medium-entropy materials as a proof-of-concept to show the effect of entropy on cycling stability. We also show that nano-level heterogeneities resulting in multiple (de-) lithiation mechanisms can lead to detrimental cycling behavior. Combined, this calls for an orchestrated approach to alloy anode engineering to improve both performance and understanding.

View Article Online
DOI: 10.1039/D6EB00032K

ARTICLE

Conversion-Alloying Electrodes for Lithium-ion Batteries: Entropy and Nano-Level Heterogeneity Effects

Received 00th January 20xx,
Accepted 00th January 20xx

DOI: 10.1039/x0xx00000x

Sajid Alvi[a], Andrea Fazi[a], Daniel Weber[b], Daniel Hedman[c], Kriti Choudhary[d], Olof Bäcke[a], Farid Akhtar[e], Jean-Noel Chotard[d,f,g], Mattias Thuvander[a], and Patrik Johansson*[a,g,]

High entropy materials promise to overcome the instability and the degradation caused by large electrode volume variations during (de-)lithiation, *i.e.* during (de-)charging of a lithium battery. Nano-level heterogeneity within such materials may, however, affect the overall performance. Here, as proof-of-concept, low (GeTe, Sb_2Te_3) and medium ((SnSbBi)Te, (SnSbBiGe)Te) entropy tellurides, as well as medium entropy composite tellurides ((SnSbBi)Te-ZnTe), (SnSbBiGe)Te-$Cu_{1.75}$Te)) have been explored for effects of entropy and heterogeneity on cycling stability and rate capability. The rate capability is shown to depend on nano-level heterogeneity rather than entropy, but the latter to be important for stable cycling; the medium entropy composite (SnSbBiGe)Te-$Cu_{1.75}$Te renders up to 140 cycles with good capacity retention (87%) and agreeable average coulombic efficiency (98.8 ± 0.4%). Altogether, characterizing and controlling nano-level heterogeneity is crucially needed to improve performance and to optimize entropy-designed alloy electrodes.

Introduction

Lithium-ion batteries (LIBs) are essential energy storage systems that today basically deliver all the performance needed for portable devices, electric vehicles, *etc* – even if improvements always are welcome. Improved energy density, both specific and volumetric, is though urged for when looking at even more demanding applications, such as electric flight.[1] In this aspect, it is crucial to develop new battery materials. While much effort within the field of LIBs has focused on cathode active materials,[2] new anode active materials, as alternatives to the omnipresent graphite, are much scarcer. The by far most popular route has been to use lithium alloying elements, such as Si, Sn, and Ge, due to their fundamentally large gravimetric lithium storage capacities.[3,4]

Recently, a tellurium-based conversion-alloying metal chalcogenide was proposed as an LIB electrode alternative, especially for microbatteries, due to the high electrical conductivity of Te: 2×10^2 S m^{-1} and the high volumetric capacity (Sb_2Te_3: 3419 mA h cm^{-3} *vs.* Si: 2041 mA h cm^{-3}).[5–7] However, its two to three structural changes during the conversion and alloying reactions can accelerate electrode pulverization, leading to fast capacity fade, continuous solid electrolyte interphase (SEI) breakdown, and particle crack generation.[5] To overcome these problems, indeed shared with all the alloying elements mentioned above, various strategies have been proposed, such as nano-engineering and compositing with various carbon materials, but as of yet no silver bullet has been found.[8–11]

High entropy materials, consisting of five or more constituent elements in (near-)equimolar compositions,[12,13] have the promise of stabilization towards pulverization,[14,15] by increased configurational entropy and thereby lowered Gibbs free energy.[16–18] This notion has been tested for high entropy oxides (HEOs) as LIB electrode materials, and indeed, entropic stabilization was initially argued during (de)lithiation.[19] However, more recently, the cation's synergetic formation of heterogenous phases of binary/ternary alloy and metal oxide(s) during cycling in HEOs, with increased electrical

---

[a] *Department of Physics, Chalmers University of Technology, SE-412 96 Gothenburg, Sweden*
[b] *Wallenberg Initiative Materials Science for Sustainability, Department of Chemistry, Chalmers University of Technology, SE-412 96 Gothenburg, Sweden*
[c] *Center for Multidimensional Carbon Materials (CMCM), Institute for Basic Science (IBS), Ulsan 44919, Korea*
[d] *Laboratoire de Réactivité et de Chimie des solides (LRCS), Université de Picardie Jules Verne, CNRS UMR7314, Amiens 80039, France*
[e] *Department of Materials Science and Mathematics, Luleå University of Technology, Luleå 97187, Sweden*
[f] *Réseau sur le stockage Electrochimique de l'Energie, CNRS FR 3459, Amiens 80039, France*
[g] *ALISTORE-European Research Institute, CNRS FR 3104, Amiens 80039, France*
**Corresponding author: patrik.johansson@chalmers.se*

View Article Online
DOI: 10.1039/D6EB00032K

conductivity, was found to be the underlying reason for enhanced cyclability.[20]

In a previous work, some of us looked at entropy stabilization via increasing entropy on both cation and anion sites of Sb_2Te_3 by studying $BiSbSe_{1.5}Te_{1.5}$ as a conversion-alloying electrode.[21] In this work, we study the effect of increasing the entropy on the cation site, in addition to exploring the effects of nano-level heterogeneity of metal telluride-based conversion-alloying electrodes. We first use density functional theory (DFT) calculations to screen for single-phase compositions by calculating the entropy forming ability (EFA) for various quaternary metal $\mathbf{Te}+\sum_i^3\mathbf{X}_i$ where $\mathbf{X}_i \in \{\mathbf{Sb},\mathbf{Sn},\mathbf{Ge},\mathbf{Bi},\mathbf{Si}\}$ systems.[22] Thereafter, one promising quaternary composition was subject to synthesis. As quaternary compositions are strictly not high, but rather medium, entropy materials,[12] we also synthesized a few quinary and senary compositions using telluride forming elements, such as Ge, Zn, and Cu, to enable us to truly explore the effects of increased entropy. Furthermore, all materials were made without compositing with any carbonaceous material, a complex procedure, and used a one-step mechanochemical process, to avoid any energy-consuming high-temperature processes.[23,24] Finally, alloy engineering via entropy and co-relating nano-level heterogeneity to battery performance can be applied to other anodes as well, especially to design less expensive compositions.

Experimental

Synthesis

All Sn (99.95%; 10 µm), Ge (99.999%; 45 µm), Zn (99.9%; 0.8 µm), and Te (99.99%; 75 µm) powders were purchased from US Research Nanomaterials Inc. (US-nano, Houston, TX, USA), while the Bi (99.5%; 45 µm) and Sb (99.5+%; 45 µm) powders were obtained from Sigma-Aldrich (Sigma-Aldrich, St. Louis, MO, USA). All powders were used without any modification and handled in an argon-filled glove-box to avoid any oxidation. The target compositions, with the abbreviations we henceforth will use within brackets, were: GeTe (GT), Sb_2Te_3 (ST), (SnSbBi)Te (SSBT), (SnSbGe)Te (SSGT), (SnSbBiGe)Te (SSBT-Ge), (SnSbBi)Te-ZnTe (SSBT-Zn), and (SnSbBiGe)Te-$Cu_{1.75}$Te (SSBT-GeCu). For the synthesis, stoichiometric amounts of reactants for each composition were ball milled using 45 ml zirconia jars and zirconia balls (⌀10 mm), with a ball-to-powder weight ratio of 20:1 (Table S1). A total of 5 g of material was processed per jar. The ball milling was performed for 50 h, with repeated steps of 10 min of milling at 600 rpm and 20 min of cooling, using a high-energy planetary ball-miller (Pulverisette 7 Premium line, Fritsch, Germany). For nano-mechanical testing, the ball-milled powders were sintered into pellets in a graphite die at 300 ˚C with a heating rate of 50 ˚C/min under vacuum (3.2 x 10^{-2} Pa) using modified spark plasma sintering (SPS) (Dr. Sinter, SPS 530ET, Fuji Electronic Industrial Co., LTD., Japan) with an integrated glove-box.

Characterization

The as-prepared materials' morphologies and compositions were characterized and analyzed using a scanning electron microscope (SEM, JEOL JSM-7800F Prime, Japan) equipped with energy-dispersive X-ray spectroscopy (EDX) using an accelerating voltage of 15 kV and a working distance of 10 mm. Powder X-ray diffraction (PXRD) was used to characterize the phases of the as-prepared materials using a D8 Discover diffractometer ($K_{\alpha1}$ and $K_{\alpha2}$, 1.54059 Å and 1.54438 Å) (Bruker Corp., MA, USA). Crystallographic phase identification and extraction of lattice parameters were performed by whole powder pattern fitting (Pawley refinements), where relevant phases and their combinations were tested to explain the observed *ex situ* PXRD patterns using the software Topas v6 (Bruker AXS). The nano-mechanical properties of the SPS made pellets were measured inside a SEM using an Alemnis indenter with a Berkovic tip (Alemnis AG, Gwatt, Switzerland). The density of the SPS made samples were measured using Archimedes' principle. Specimens for atom probe tomography (APT) were lifted out from powder particles inside the electrode coated on a Cu current collector using a dual beam workstation equipped with SEM and focused-ion beam (FIB) (Versa3D, FEI, Hillsboro, Oregon, USA). Conventional APT lift-out procedures were adapted to powder embedded in matrix (Figure S1).[25,26] An accelerating voltage of 30 kV was used for the ion beam, and currents of 15 – 1 nA and 100 µA, were used for rough milling and shaping, respectively. Final polishing of the tips was performed using 2 kV acceleration voltage and 48 pA current. APT specimens were obtained from fresh electrodes and electrodes after 3 full cycles and measurements were carried out using a LEAP 6000 XR (CAMECA, Gennevilliers, France) with the following run parameters: 35 K specimen temperature, 30 pJ laser pulse energy, 0.3% evaporation rate, and auto pulse rate control set to guarantee a minimum mass spectrum range of 550 Da. *Operando* XRD was done using the D8 Discover diffractometer, a rotating anode diffractometer from Bruker, and a newly designed *operando* cell (LeRiChe'S Cell v2)

View Article Online
DOI: 10.1039/D6EB00032K

equipped with a beryllium window.[27] The measurements were performed with coated electrodes of active material loading of 4 mg/cm^2 in transmission mode using the same method as described in Section 4.4.

Modelling

EFA descriptors were calculated for all quaternary metal tellurides compositions, $\mathbf{Te} + \sum_i^3 \mathbf{X}_i$ where $\mathbf{X}_i \in \{\mathbf{Sb},\mathbf{Sn},\mathbf{Ge},\mathbf{Bi},\mathbf{Si}\}$, making 10 systems in total, by the approach developed by Sarker *et al.*,[22] with one modification: the enthalpies (formation energies) for the unique supercells generated by the automatic flow partial occupation (AFLOW-POCC) algorithm[28] were computed using the Materials Project database[29] (version v2021.11.10) rather than AFLOW,[30] as previously.[31] From the AFLOW inputs (PARTCAR files) derived from the α-arsenic unit cell, the AFLOW-POCC algorithm generated 215 unique supercells, each containing 8 atoms, for each quaternary composition (4300 supercells in total).

The total energies, $\boldsymbol{E}_{\mathbf{tot}}$, of these unique supercells were obtained via DFT calculations using the Vienna Ab initio Simulation Package (VASP) version 6.3.0.[32–34] Our calculations employed a plane wave basis set, the projector-augmented wave (PAW) method,[35,36] and the Perdew-Burke-Ernzerhof (GGA-PBE) exchange-correlation functional.[37] To ensure compatibility with the Materials Project database, we used a plane-wave energy cut-off of 520 eV, a k-point density of 0.20 Å^{-1} (KSPACING = 0.20), and the common choice of pseudopotentials. For all calculations, the electronic self-consistent loop was converged to an energy tolerance of 10^{-6} eV, with no symmetry constraints (ISYM = 0), high precision (PREC = Accurate) and with aspherical contributions to the Kohn-Sham potential included (LASPH = True). The Methfessel–Paxton scheme[38] (ISMEAR = 1) was used for partial occupancies, with a smearing width of 0.1 eV and all calculations were non-spin-polarized (ISPIN = 1). Each unique supercell was relaxed in three sequential steps. First, the cell volume was relaxed while keeping the cell shape fixed (ISIF = 7) until the change in total energy between two consecutive steps was below 10^{-3} eV (EDIFFG = 1.0E-3). Subsequently, a rough full relaxation was performed (ISIF = 3) using the conjugate gradient method (IBRION = 2), with a force convergence criterion of 10^{-2} eV/Å (EDIFFG = -1.0E-2). Finally, an accurate full relaxation was performed using the quasi-Newton method (IBRION = 2) with the same convergence criteria.

After relaxation the formation energy, $\boldsymbol{E}_{\boldsymbol{f},\boldsymbol{i}}$, for each unique supercell, $\boldsymbol{i}$, was calculated as $\boldsymbol{E}_{\boldsymbol{f},\boldsymbol{i}} = \boldsymbol{E}_{\mathbf{tot},\boldsymbol{i}} - \sum_{\boldsymbol{j}=\mathbf{1}}^{\mathbf{4}} \boldsymbol{n}_{\boldsymbol{j}}\, \boldsymbol{E}_{\boldsymbol{j}}$, where $\boldsymbol{n}_{\boldsymbol{j}}$ is the number of atoms of element *j* in the unique supercell $\boldsymbol{i}$ and $\boldsymbol{E}_{\boldsymbol{j}}$ is the energy per atom of element $\boldsymbol{j}$ obtained from the Materials Project database. The EFA descriptor, $\boldsymbol{\sigma}_{\boldsymbol{E}_{\boldsymbol{f}}}$, for each compound was then calculated from the formation energy, $\boldsymbol{E}_{\boldsymbol{f}}$, as

$$\boldsymbol{\sigma}_{\boldsymbol{E}_{\boldsymbol{f}}} = \sqrt{\frac{\sum_i \boldsymbol{g}_i \left(\boldsymbol{E}_{\boldsymbol{f},\boldsymbol{i}} - \boldsymbol{E}_{\boldsymbol{f}}^{\mathbf{mix}}\right)^{\mathbf{2}}}{\sum_i \boldsymbol{g}_i - \mathbf{1}}} \text{ with } \boldsymbol{E}_{\boldsymbol{f}}^{\mathbf{mix}} = \frac{\sum_i \boldsymbol{g}_i\, \boldsymbol{E}_{\boldsymbol{f},\boldsymbol{i}}}{\sum_i \boldsymbol{g}_i},$$

where $\boldsymbol{g}_{\boldsymbol{i}}$ is the degeneracy of each unique supercell $\boldsymbol{i}$ obtained via the AFLOW-POCC algorithm.

Electrode manufacturing and battery performance tests

Electrodes were prepared by mixing the active material (70 wt.%) with Super P carbon (20 wt.%), sodium carboxymethyl cellulose (CMC, 5 wt.%), and styrene butadiene rubber (SBR, 5 wt.%) in deionized water using a magnetic stirrer. The slurry was subsequently cast onto copper foil (17 µm, Schlenk Metallfolien GmbH & Co. KG, Germany) and dried at 80 °C in a vacuum oven for 12 h. Electrodes (⌀13 mm) were cut out and further dried in vacuum at 80 ^{o}C for 12 h. The mass loading of active material was fixed and limited to 1.5-2.0 mg cm^{-2} (due to crack formation in coatings with higher active material mass loadings). Coin cells (CR2032) were assembled in an argon-filled glove-box using as-received lithium metal (0.2 mm thickness, ⌀14 mm , purity >99.8%, Honjo Metals, OSK, Japan) as counter electrode, a glass fibre separator (420 µm thickness, Whatman GF/C, GE Healthcare), and 70 µL of 1 M LiPF$_6$ dissolved in ethylene carbonate (EC) and ethylmethylene carbonate (EMC) (30:70, by wt.%) with 10 wt.% FEC (E-lyte Innovations GmbH, Münster, Germany) electrolyte. Galvanostatic discharge/charge cycling (GC) tests were performed between 0.01 and 3 V *vs.* Li$^+$/Li^o at C/5 rate at room temperature (22 °C) using a battery test system (Scribner 585, NC, USA). The theoretical capacity was calculated based on at.% of active material used to create each compound (see Table S2).

Results and Discussion

First, to guide our synthesis efforts, the EFAs were calculated, whereafter the quaternary composition with the highest EFA showing a single phase was synthesized alongside some quinary and

View Article Online
DOI: 10.1039/D6EB00032K

senary variants. To further correlate the calculated EFA to single-phase formation, the quaternary telluride with the second highest EFA was also synthesized. Subsequently, the PXRD patterns of synthesized tellurides were matched *vs.* known crystal structures by Pawley fitting and characterized with respect to morphology via SEM. Thereafter, the electrochemical properties were assessed in lithium half-cells and correlated with the compositional entropy and the nano-level heterogeneity using APT. The electrode structural evolution was studied using *operando* XRD for four charge-discharge cycles. Finally, we conducted *post* mortem analysis of our cycled electrodes.

Quaternary telluride stabilities and synthesis selection

The EFA descriptor is used to predict the likelihood of forming a single-phase quaternary telluride – the higher the EFA, the greater the tendency to form a stable single-phase. Here, the highest EFA value obtained is 33.1 eV^{-1} (Table 1), which is lower than the ~50 eV^{-1} EFA threshold used to predict single phase for high-entropy carbides.[22] Other commonly cited EFA thresholds include ~40 eV^{-1} for high-entropy carbonitrides and ~80 eV^{-1} for borides.[39] However, the radically different compositions and bonding nature of our tellurides make such a direct comparison questionable. Instead, we simply tried to experimentally synthesize (SnSbBi)Te (SSBT) and (SnSbGe)Te (SSGT), and indeed, a single-phase SSBT and SSGT were obtained. After this, with SSBT as a base, the (SnSbBiGe)Te (SSBT-Ge), (SnSbBiZn)Te (SSBT-Zn) and (SnSbBiGeCu)Te (SSBT-GeCu) compounds, with larger entropy of assembly, were the subject of synthesis efforts.

Table 1. The DFT-derived EFA for ten quaternary compositions.

Composition	EFA σ_{E_f} (eV^{-1})
SnSbBiTe	33.1
SnSbGeTe	26.0
SnBiGeTe	24.6
SbBiGeTe	24.0
SnSbSiTe	17.6
SbBiSiTe	16.8
SnBiSiTe	15.9
SnGeSiTe	14.5
SbGeSiTe	14.31
BiGeSiTe	11.83

Structure and morphology

Turning to the structures of the synthesized materials, the PXRD patterns of SSBT and its increased entropy variants (SSBT-Ge, SSBT-Zn, and SSBT-GeCu) were indexed in the space group *R*-3*m,* similar to that of low-entropy ST (Figure 1). In addition, significant fractions of the intensities in the PXRD patterns of SSBT-Zn and SSBT-GeCu necessitated the addition of ZnTe and $Cu_{1.75}Te$ as secondary phases, respectively. Similarly, the presence of nanocrystalline GeO_2 is observed in SSBT-Ge (Figure 1d), which was indexed after observing the evidence of nano-level heterogeneity (see Section 3.4). The presence of secondary phases suggests limited solubility of Ge, Zn and Cu in SSBT (Figures 1e-f). The *a* lattice parameters of SSBT-Ge and SSBT-Zn phases (space group: *R*-3*m*H) increased with respect to that of SSBT, suggesting lattice distortion arising from increased entropy (Table S3). Also, the SPS made SSBT and SSBT-Ge showed formation of the *R*-3*m* phase, with an additional well-crystallized GeO_2 phase for the latter (Figure S2). In contrast, a small amount of GeO_2 phase is present in the ball-milled SSBT-Ge (Figure 1d), which can be related to its presence as a nanocrystalline material that crystallized after SPS. Furthermore, the additional quaternary telluride of SSGT, with the second-highest EFA value, also showed the formation of a single phase with *R*-3*m*H space group, which correlates well with the EFA prediction (Table 1; Figure S3). In terms of morphology, the particle sizes of the ball-milled materials range from 0.5 to 3 µm with a uniform elemental distribution, although differing in at.% from the starting composition, which can be due to material loss(es) or nano-level heterogeneity (Figures 2; Figure S4 and Table S4).

View Article Online
DOI: 10.1039/D6EB00032K

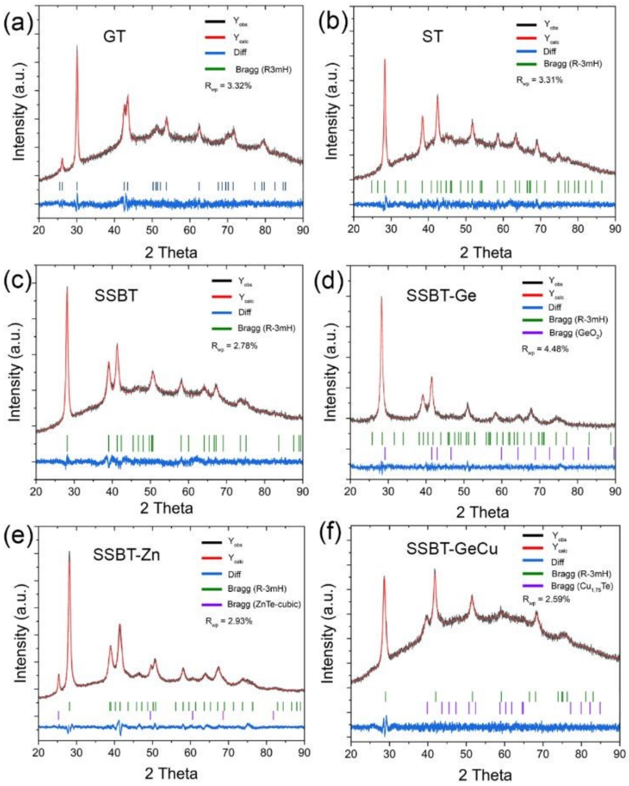

Fig. 1. X-ray diffractograms of the synthesized metal tellurides.

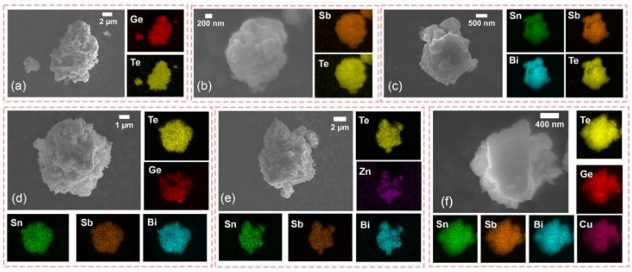

Fig. 2. SEM with EDX mapping of a) GT, b) ST, c) SSBT, d) SSBT-Ge, e) SSBT-Zn, and f) SSBT-GeCu.

Electrochemical assessment and battery performance

Using lithium half-cells, the (de-)lithiation of low entropy ST and GT rendered typical conversion (Li_2Te) and alloying (Li_xSb/Li_xGe) signatures during the first lithiation stage, followed by de-alloying and re-conversion (Figures 3a,e; Figure S5).[9] In the following cycles, the lithiation behavior changed to mainly being alloying, suggesting irreversible formation of ST and GT. As we increase the entropy by moving to SSBT, we observe a two-step lithiation in the 1st cycle with conversion and alloying reactions to form Li_2Te and Li_xSb/Li_xBi/Li_xSn, respectively (Figures 3b,f). The single alloying peak can be related to the simultaneous alloying of Sb, Bi, and Sn, as reported previously for lithiation of TiSnSb.[40] For the subsequent cycles, the conversion peak potential increases, most probably due to the SEI formed during the 1st cycle.[11,41] The presence of additional peaks during lithiation (1.7 V *vs.* Li^+/Li°) and de-lithiation (1.84 V *vs.* Li^+/Li°) suggests possible intermediate polytelluride phases until Li_2Te phase is formed.[6] In the following cycles, the single alloying peak at 0.77 V splits into three separate peaks, corresponding to the alloying reactions of Li_xSb, Li_xBi and Li_xSn, respectively.[41–43] A similar behavior was observed for SSBT-Ge and SSBT-Zn (Figures 3c,g and S6a-b) and further increasing the entropy by moving to SSBT-GeCu, the single conversion and alloying peaks are maintained even for the 20th cycle, along with lower polarization after the 90th cycle, strongly suggesting an entropy-driven reversibility (Figures 3d,h). Thus, the long-term cycling stability can be related to less volume expansion during lithiation, this as each Li_xA (A: Sn, Sb, Bi, Zn, Ge, Te) compound can provide a buffering effect.[44] Furthermore, a recent computational study showed that CuTe may further stabilize the cycling behavior, due to its high conductivity and balanced spin states, providing stable lithium-ion adsorption, and as a result render cycling stability of SSBT-GeCu.[6] In contrast to SSBT, SSGT displayed two distinct alloying peaks, indicating a different lithiation behavior (Figure S7a-b). These peaks can be attributed to the significant lithiation potential differences between Sn (0.4–0.7 V), Sb (0.78–0.99 V), and Ge (0.25–0.4 V), as well as the higher Ge content in SSGT. Notably, the conversion peaks in SSGT nearly disappear after the 10th cycle, suggesting an irreversible conversion reaction. This behavior is likely due to its lower EFA as compared to SSBT, which impedes the reformation of a single phase after delithiation in the first cycle, resulting in a larger presence of irreversible Li_2Te phase (Figure S8).

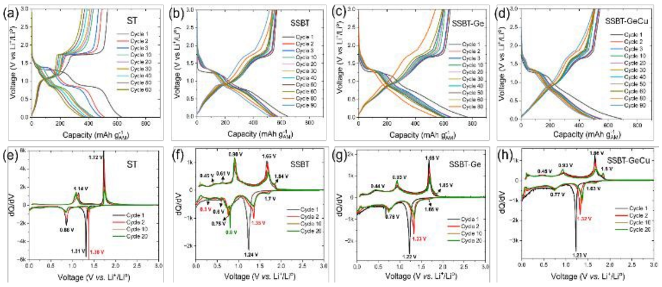

Fig. 3. GC and dQ dV^{-1} for: a,e) ST, b,f) SSBT, c,g) SSBT-Ge, and d,h) SSBT-GeCu at C/5 rate.

Turning to battery cycling performance, the low entropy ST and GT show severe capacity fading after a mere 10-20 cycles (Figure 4a). Somewhat surprisingly, SSBT-Ge shows worse capacity retention than SSBT, but this can be correlated with the lower hardness (1.6 ± 0.4 GPa) and Young's modulus (36.8 ± 3.2 GPa) of the latter, as compared to both SSBT-Ge (2.1 ± 0.4 GPa and 42 ± 3.5 GPa) and Sb_2Te_3 (2.3 ± 0.2 GPa and 56.5 ± 4.2 GPa) (Figures 4b; Figure S9), as a result giving low stiffness for SSBT and may enhance the buffering-effect during the 1st lithiation.[45,46] Furthermore, SSBT shows a high volumetric capacity of ~3100 mAh cm^{-3} after 75 cycles (Figure S10). SSBT-Zn shows similar capacity retention to SSBT (Figure S6c), while the SSBT-GeCu shows the highest capacity retention (87%) and agreeable average coulombic efficiency (CE) (98.8 ± 1.8 %) for 140 cycles (Figure 4a). In addition, SSBT-GeCu showed the same performance even under leaner electrolyte conditions, suggesting no large contributions of electrolyte degradation side-reactions (Figure S11). The higher capacity retention, at least for 70 cycles, can also be related to the presence of Bi, whose intermediate lithiation potential (~0.73 – 0.78 V) to form Li_3Bi can act as a buffer phase, in addition to Li_2Te and Li_3Sb, for elements with lower lithiation potential (Sn, Zn, and/or Ge). This can be deduced from the lower capacity retention of SSGT, having no Bi (Figure S7c).

The effect of increased entropy on the cycling stability can also be inferred from the relative CE differences, rather than the absolute CEs (Figure S12), whereas SSBT-GeCu maintains a more stable CE for all its 140 cycles. In addition to the entropy-driven reversibility, the inactive nature of Cu in SSBT-GeCu can further provide structural stability during (de-)lithiation. Furthermore, the $Cu_{1.75}Te$ secondary phase in SSBT-GeCu shows a positive effect, possibly due to the synergetic effect of the telluride-based composite or the formation of a new inactive alloy phase during cycling with good electrical/mechanical properties.[6,20] In contrast to the capacity retention, the rate capability was found to be superior for SSBT (Figures 4c; Figure S6d; and Figure S7d), likely due to the absence of any nano-level heterogeneity (see Section 3.4).

View Article Online
DOI: 10.1039/D6EB00032K

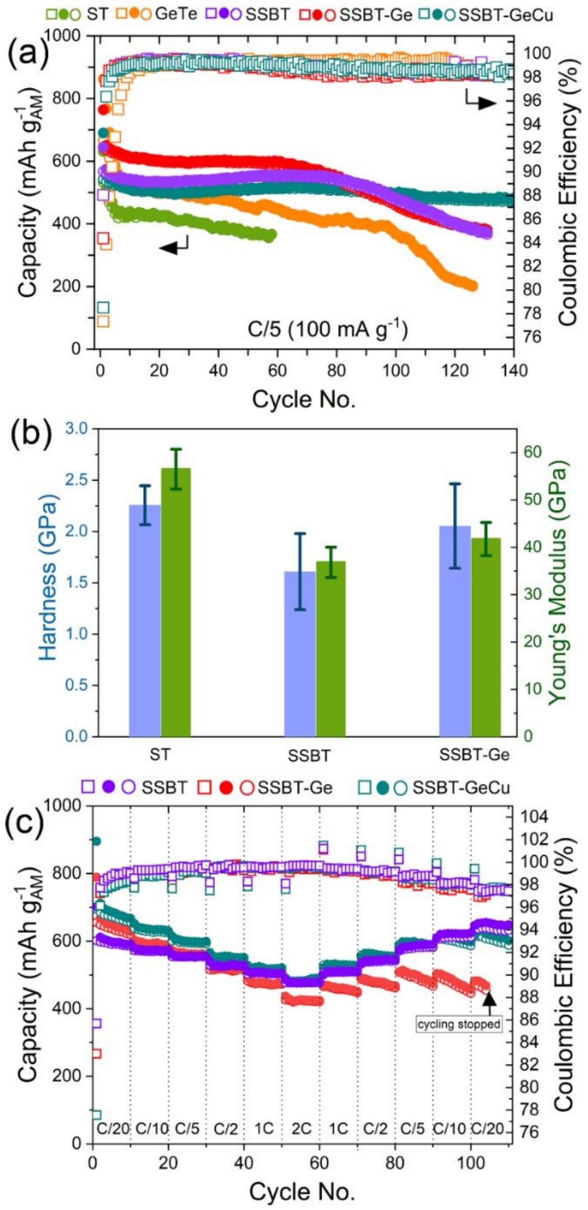

Fig. 4. (a) Cycling performance, b) mechanical properties, and c) rate performance of as-prepared metal telluride electrodes in half-cells. (Symbols in (a) and (c): closed circle is discharge capacity, open circle is charge capacity, and open rectangle is CE)

Nano-level heterogeneity

Above the unexpected lower capacity retention of SSBT-Ge as compared to SSBT was correlated with mechanical properties. Using APT we also found fresh SSBT-Ge to show a large amount of nano-level heterogeneity, *i.e.* 1-10 nm sized GeO_2 domains embedded in a

View Article Online
DOI: 10.1039/D6EB00032K

homogeneous SSBT-Ge matrix (Figure 5a), a matrix that in turn has a non-equiatomic stoichiometry. Minor nanocrystalline nano-level heterogeneity was detected by XRD (Figure 1d), due to the nanocrystalline nature of GeO_2. The formation of GeO_2 can be due to a combination of the highly reactive nature of Ge nanoparticles and a small amount of oxygen trapped in the milling jars during the powder preparation, despite being made inside the glove-box. During lithiation, the GeO_2 domains possibly go through a conversion reaction (eq. 1) as well as an alloying reaction (eq. 2) (in addition to the alloying-conversion reaction of the SSBT-Ge matrix):

$$2Li^{+} + 2e^{-} + {}^{1}/_{2}\, GeO_2 \rightarrow Li_2O + {}^{1}/_{2}\, Ge \quad (eq. 1)$$

$$xLi^{+} + Ge + xe^{-} \rightarrow Li_xGe \quad (eq.2)$$

And indeed: the APT of SSBT-Ge after 3 charge-discharge cycles show a large part of the Li (amounting to 30-75 at.%) being trapped in the GeO_2 domains (Figure 5b). In addition, the GeO_2 domain size increased from ~1-10 nm to ~5-20 nm, exacerbated by substantial accumulation of Li at the former GeO_2-matrix interface. This further increases the irreversible capacity losses in SSBT-Ge and the electrode volume expansion upon lithiation, and thereby possibly causes electrode pulverization. Yet, no lithiation signature of GeO_2 was found by the dQ dV^{-1} analysis, possibly due to the low absolute amount (Figure 3g). The APT of SSBT-Zn show formation of two phases: SSBT-Zn and ZnTe (Figure S13a), and similarly to the case of SSBT-Ge, a large amount of lithium was found in ZnTe after cycling (Figure S13b). In addition, small amounts of isolated pure Sb particles were also observed, suggesting the irreversibility of the SSBT-Zn matrix phase (after three cycles). Hence, the better rate performance of both SSBT-Zn and SSBT-GeCu as compared to SSBT-Ge (Figure 4c; Figure S6d) suggests that the existence of composite phases (ZnTe and $Cu_{1.75}Te$, respectively) with similar lithiation behavior to SSBT-matrix can overcome the issues caused by nano-level heterogeneity by a different phase (GeO_2) present, as in SSBT-Ge. In addition, the presence of Ge in SSBT-GeCu did not have any adversary effect on cycling and rate capability, as compared to for SSBT-Ge. This may be due to the absence of GeO_2 (Figure 2d), which in turn is due to less Ge in the overall composition.

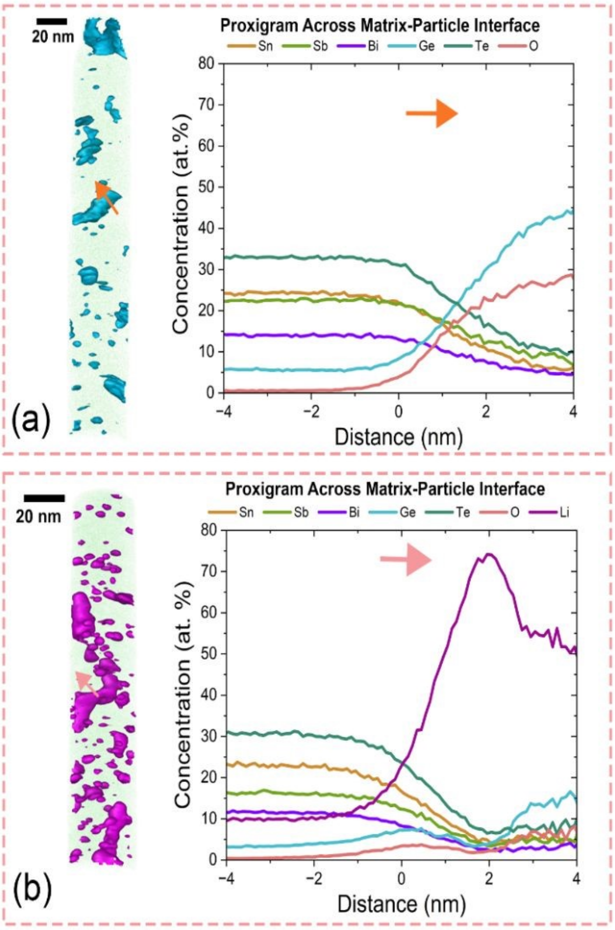

Fig. 5. APT 3D reconstructions and proximity histogram composition plots of SSBT-Ge from: a) fresh electrode, and b) after 3 cycles at C/5 in a half-cell. Sn atoms are plotted in green to outline the tip shape, the Ge isosurface set at 7.5 at.% is plotted in light blue (fresh electrode) and the Li isosurface set at 25 at.% is plotted in magenta (3 full cycled electrode).

Operando and *ex situ* structural evolution

The *operando* XRD measurements were performed to further understand the structural changes and (de)-lithiation mechanism during cycling. The onset of lithiation in SSBT leads to a shift in the diffraction peaks towards lower angles and thus increased unit cell volumes, suggesting lithium incorporation into the hexagonal structure and that Li_2Te is formed, as evidenced by broad peaks at 2 theta of *ca.* 10.75°, 12.4°, and 17.4° (Figure 6a). These peaks disappear at the onset of the alloying reaction (at *ca.* 1 V) and then appear again at the end of the alloying reaction (at *ca.* 0.6 V). The absence of any of the expected alloying peaks, from compounds such as Li_xBi, Li_xSn, or Li_xSb suggests the formation of nano-crystalline or amorphous domains, which have been reported previously for ternary-selenide and -telluride compounds.[24,47] After the end of the re-conversion reaction in the first cycle, the peaks of the SSBT phase reappear, but the peaks are too broad to allow us to obtain any lattice parameters information. Second, the *operando* XRD assessment of SSBT-Ge and SSBT-Zn showed a similar cycling behavior (Figure 6b; Figure S14). In contrast, *ex situ* XRD of the lithiated SSGT electrode showed presence of crystalline phases from lithium-alloying (Li$_{15}$Ge$_4$, Li$_7$Ge$_{12}$, and Li$_3$Sb), and it became amorphous after delithiation with addition of the presence of an irreversible Li$_2$Te phase (Figure S8). The latter correlates well with the absence of conversion reactions after a mere 3 cycles (Figure 7b).

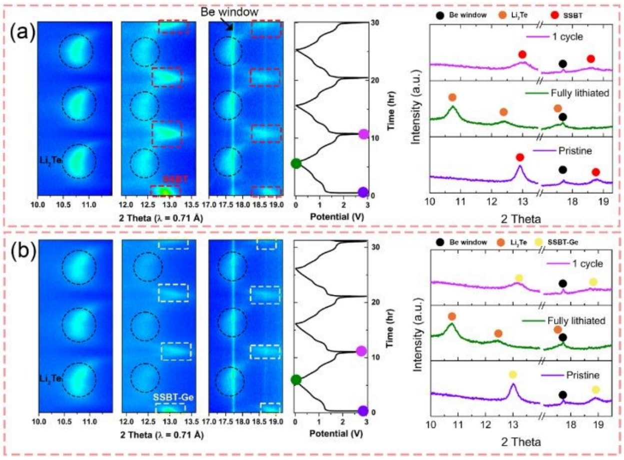

Fig. 6. *Operando* XRD of: a) SSBT, and b) SSBT-Ge, in half-cells at C/5 rate.

Post mortem evaluation

The *post mortem* SEM of electrodes after more than a hundred cycles showed a larger expansion of the active material particles of medium entropy SSBT and SSBT-Ge (Figures 7a-b and 7c-d, respectively) as compared to medium entropy SSBT-GeCu composite (Figures 7e-f). The increased entropy and the synergy of the secondary phase (Cu$_{1.75}$Te) in SSBT-GeCu seem to suppress the particle expansion, and thereby hopefully also prevents electrode pulverization, which correlates well with its higher capacity retention (Figure 4a). Nonetheless, no cracks were actually observed in any of these electrodes. However, to make clear the role of entropy, and in stark contrast, the *post mortem* SEM of the low entropy ST electrode indeed showed a large amount of cracks in the coating and the particles after a mere 60 cycles (Figures 7g-h).

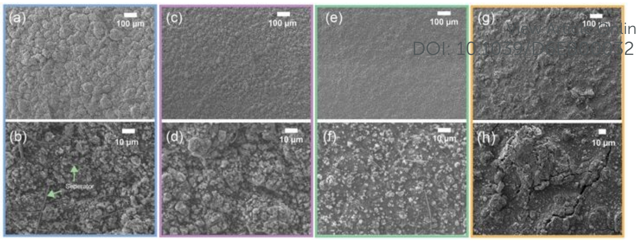

Fig. 7. *Post mortem* SEM of electrodes: (a-b) SSBT (after 130 cycles), (c-d) SSBT-Ge (after 130 cycles), (e-f) SSBT-GeCu (after 140 cycles), and (g-h) ST (60 cycles).

Summary

We have explored the effects of entropy and nano-level heterogeneity on the (de-)lithiation behavior of different metal telluride LIB electrodes. We were able to enhance the electrochemical cycling stability by a factor of ten for the medium entropy composite SSBT-GeCu as compared to the low entropy GT and ST. The enhancement of both the capacity retention (87%) and the average CE (98.8%) in SSBT-GeCu showed that increased entropy can overcome nano-level heterogeneity, if the so-created composite phase has a similar structure as the matrix phase. However, for the rate performance, nano-level homogeneity takes precedence even for alloys with increased entropy. We also show that the use of XRD and SEM/EDX is not enough as non-visible nano-level heterogeneity can anyhow lead to detrimental effects on the battery cycling performance – why APT characterization is crucial for multimetallic alloys.

Author contributions

Sajid Alvi: conceptualization, methodology, software, data curation, visualization, writing – original draft, writing – review & editing. Andrea Fazi: methodology, data curation, writing – review & editing. Daniel Weber: data curation, writing – original draft, writing – review & editing. Daniel Hedman: methodology, data curation, writing – review & editing. Kriti Choudhary: data curation, writing – review & editing. Olof Bäcke: data curation, writing – review & editing. Farid Akhtar: data curation, visualization, writing – original draft, writing – review & editing. Jean-Noel Chortard: data curation, writing – review & editing. Mattias Thuvandera: methodology, writing – review & editing. Patrik Johansson: visualization, methodology, funding acquisition, supervision, writing – review & editing.

View Article Online
DOI: 10.1039/D6EB00032K

Conflicts of interest

There are no conflicts to declare.

Data availability

The data supporting the findings of this study are available from the corresponding author upon reasonable request. Supplementary information (SI) is available.

Acknowledgements

SA and PJ acknowledge the financial support from the Area of Advance Production of Chalmers University of Technology and the Swedish Research Council's Distinguished Professor grant #2021-00613 on Next Generation Batteries to PJ. DW acknowledges the financial support from Wallenberg Initiative Materials Science for Sustainability (WISE), funded by the Knut and Alice Wallenberg Foundation.

References

1 T. Kim, W. Song, D.-Y. Son, L. K. Ono and Y. Qi, *J. Mater. Chem. A Mater.*, 2019, **7**, 2942–2964.

2 A. Manthiram, *Nat. Commun.*, 2020, **11**, 1–9.

3 W. J. Zhang, *J. Power Sources*, 2011, **196**, 13–24.

4 J. Yang, S. Wang, S. Song, D. An, X. Yu, Q. Zhu, D. Yu, J. Wang, S. Dong, J. Nai, J. Yang, Z. Ma, M. Kurbanov, B. Gao and H. Wang, *Advanced Materials*, 2025, **37**, 2501807.

5 H. Fan, P. Mao, H. Sun, Y. Wang, S. S. Mofarah, P. Koshy, H. Arandiyan, Z. Wang, Y. Liu and Z. Shao, *Mater. Horiz.*, 2022, **9**, 524–546.

6 M. Bhatt, H. Park, S. Kansara, Y. Sonvane and J. Y. Hwang, *ACS Appl. Mater. Interfaces*, 2025, **17**, 4884–4894.

7 L. Zhang, Z. Yang, S. Feng, Z. Guo, Q. Jia, H. Zeng, Y. Ding, P. Das, Z. Bi, J. Ma, Y. Fu, S. Wang, J. Mi, S. Zheng, M. Li, D. M. Sun, N. Kang, Z. S. Wu and H. M. Cheng, *Nature*, 2024, **628**, 313–319.

8 S. Y. Son, J. Hur, K. H. Kim, H. Bin Son, S. G. Lee and I. T. Kim, *J. Power Sources*, 2017, **365**, 372–379.

9 K. H. Nam, G. K. Sung, J. H. Choi, J. S. Youn, K. J. Jeon and C. M. Park, *J. Mater. Chem. A Mater.*, 2019, **7**, 3278–3288.

10 D. Sun, G. Zhang, D. Li, S. Liu, X. Jia and J. Zhou, *Sustain. Energy Fuels*, 2019, **3**, 3163–3171.

11 W. Zhang, Q. Zhang, Q. Shi, S. Xin, J. Wu, C. L. Zhang, L. Qiu and C. Zhang, *ACS Appl. Mater. Interfaces*, 2019, **11**, 29934–29940.

12 E. P. George, D. Raabe and R. O. Ritchie, *Nat. Rev. Mater.*, 2019, **4**, 515–534.

13 S. Alvi, M. Milczarek, D. M. Jarzabek, D. Hedman, M. G. Kohan, N. Levintant-Zayonts, A. Vomiero and F. Akhtar, *Adv. Eng. Mater.*, 2022, **9**, 2101626.

14 L. Lin, K. Wang, A. Sarkar, C. Njel, G. Karkera, Q. Wang, R. Azmi, M. Fichtner, H. Hahn, S. Schweidler and B. Breitung, *Adv. Energy Mater.*, 2022, **12**, 2103090.

15 X. Li, J. H. Wang, L. Yang, T. Y. Liu, S. Huang, B. Ho, H. Hsueh, J. Chen, L. He, Z. Guo, M. Liu and W. Li, *Advanced Materials*, 2024, **36**, 2409278.

16 M. Fu, X. Ma, K. Zhao, X. Li and D. Su, *iScience*, 2021, **24**, 102177.

17 Y. Wang, H. Lan, S. Dong, Q. Zhu, L. Cheng, H. Wang, J. Wang, S. Wang, M. Tang, K. M. Shodievich, G. Wang and H. Wang, *Adv. Funct. Mater.*, 2024, **34**, 2315498.

18 Y. Li, J. Wang, Y. Wang, S. Wang, L. Wu, B. Zhou, D. Yang, L. Jiang, L. Kan, Q. Zhu, M. Kurbanov and H. Wang, *Advanced Materials*, 2025, **37**, 2419764.

19 A. Sarkar, L. Velasco, D. Wang, Q. Wang, G. Talasila, L. de Biasi, C. Kübel, T. Brezesinski, S. S. Bhattacharya, H. Hahn and B. Breitung, *Nat. Commun.*, 2018, **9**, 3400.

20 K. Wang, W. Hua, X. Huang, D. Stenzel, J. Wang, Z. Ding, Y. Cui, Q. Wang, H. Ehrenberg, B. Breitung, C. Kübel and X. Mu, *Nat. Commun.*, 2023, **14**, 1–9.

21 S. Alvi, A. P. Black, I. Jozami, C. Escudero, F. Akhtar and P. Johansson, *Batter. Supercaps*, 2024, **7**, e202300585.

22 P. Sarker, T. Harrington, C. Toher, C. Oses, M. Samiee, J.-P. Maria, D. W. Brenner, K. S. Vecchio and S. Curtarolo, *Nat. Commun.*, 2018, **9**, 4980.

23 N. Mahmood, T. Tang and Y. Hou, *Adv. Energy Mater.*, 2016, **6**, 1600374.

24 Y. Zhu, J. Zhao, L. Li, J. Mao, J. Xu and J. Jin, *Chem. Eng. Sci.*, 2020, **225**, 1–9.

25 P. P. Choi, Y. S. Kwon, J. S. Kim and T. Al-Kassab, *J. Electron Microsc. (Tokyo).*, 2007, **56**, 43–49.

26 K. Thompson, D. Lawrence, D. J. Larson, J. D. Olson, T. F. Kelly and B. Gorman, *Ultramicroscopy*, 2007, **107**, 131–139.

View Article Online
DOI: 10.1039/D6EB00032K

27 K. Choudhary, I. O. Santos Mendoza, A. Nadeina, D. Becker, T. Lombard, V. Seznec and J.-N. Chotard, *J. Power Sources*, 2023, **553**, 232270.

28 K. Yang, C. Oses and S. Curtarolo, *Chemistry of Materials*, 2016, **28**, 6484–6492.

29 A. Jain, S. P. Ong, G. Hautier, W. Chen, W. D. Richards, S. Dacek, S. Cholia, D. Gunter, D. Skinner, G. Ceder and K. A. Persson, *APL Mater.*, 2013, **1**, 011002.

30 S. Curtarolo, W. Setyawan, G. L. W. Hart, M. Jahnatek, R. V. Chepulskii, R. H. Taylor, S. Wang, J. Xue, K. Yang, O. Levy, M. J. Mehl, H. T. Stokes, D. O. Demchenko and D. Morgan, *Comput. Mater. Sci.*, 2012, **58**, 218–226.

31 D. Hedman, A. C. Feltrin, Y. Miyamoto and F. Akhtar, *J. Mater. Sci.*, 2022, **57**, 422–443.

32 G. Kresse and J. Hafner, *Phys. Rev. B*, 1993, **47**, 558–561.

33 G. Kresse and J. Furthmüller, *Comput. Mater. Sci.*, 1996, **6**, 15–50.

34 G. Kresse and J. Furthmüller, *Phys. Rev. B*, 1996, **54**, 11169–11186.

35 P. E. Blochl, *Phys. Rev. B*, 1994, **50**, 17953–17979.

36 G. Kresse and D. Joubert, *Phys. Rev. B*, 1999, **59**, 1758–1775.

37 J. P. Perdew, K. Burke and M. Ernzerhof, *Phys. Rev. Lett.*, 1996, **77**, 3865–3868.

38 M. Methfessel and A. T. Paxton, *Phys. Rev. B*, 1989, **40**, 3616–3621.

39 S. Divilov, H. Eckert, D. Hicks, C. Oses, C. Toher, R. Friedrich, M. Esters, M. J. Mehl, A. C. Zettel, Y. Lederer, E. Zurek, J. P. Maria, D. W. Brenner, X. Campilongo, S. Filipović, W. G. Fahrenholtz, C. J. Ryan, C. M. DeSalle, R. J. Crealese, D. E. Wolfe, A. Calzolari and S. Curtarolo, *Nature*, 2024, **625**, 66–73.

40 M. T. Sougrati, J. Fullenwarth, A. Debenedetti, B. Fraisse, J. C. Jumas and L. Monconduit, *J. Mater. Chem.*, 2011, **21**, 10069–10076.

41 Y. Wei, J. Chen, S. Wang, X. Zhong, R. Xiong, L. Gan, Y. Ma, T. Zhai and H. Li, *ACS Appl. Mater. Interfaces*, 2020, **12**, 16264–16275.

42 S. Wen, J. Zhao, Y. Zhu, J. Mao, H. Wang and J. Xu, *J. Alloys Compd.*, 2020, **837**, 155536.

43 S. Y. Son, J. Hur, K. H. Kim, H. Bin Son, S. G. Lee and J. T. Kim, *J. Power Sources*, 2017, **365**, 372–379.

44 J. Zhao, Z. Wei, N. Chen, F. Meng, R. Tian, Y. Zeng and F. Du, *Energy Storage Mater.*, 2024, **65**, 103127.

45 C. S. Hong and S. M. Han, *Extreme Mech. Lett.*, 2020, **40**, 100907.

46 H. Kang, H. Kang, J. Piao, X. Xu, Y. Liu, S. Xiong, S. Lee, H. Kim, H.-G. Jung, J. Kim, Y.-K. Sun and J.-Y. Hwang, *Small Methods*, 2024, **8**, 2301158.

47 D. Hui, X. Chen, X. Bian, C. He, S. Yao, G. Chen and F. Du, *Chemistry – A European Journal*, 2023, **29**, e202203044.

View Article Online
DOI: 10.1039/D6EB00032K

Data availability

The data supporting the findings of this study are available from the corresponding author upon reasonable request. Supplementary information (SI) is available.